Concentric-Annulus Electrical Capacitance Tomography Sensors

Jiamin Ye, Haigang Wang, Ruihuan Ge and Wuqiang Yang

Abstract—The aim of this research is to investigate a unique shape (concentric annulus) electrical capacitance tomography (ECT) sensors and to investigate the measurement strategies. This is motivated by the desire to improve the contrast and spatial resolution of the images reconstructed using ECT with internal-external electrodes (IEE). Both numerical simulation and experimental study were carried out, with the goal of providing an improved understanding of the configuration of IEE sensors, the internal shield and the measurement strategies. Simulation results are in agreement with the experimental results. Using liner back projection algorithm, the IEE sensor with 12 external electrodes and 4 internal electrodes with the external-opposite-internal measurement strategy can reconstruct high quality images. The internal shield has almost no effect on the imaging quality.

Index Terms—Electrical capacitance tomography, capacitance sensor, internal-external electrode, numerical simulation, experimental study.

I. Introduction

Granulation, coating and drying processes are common in the pharmaceutical industry. It is important to understand the hydrodynamic behavior of gas-solids two phase flows in a fluidized bed for controlling these processes and the quality of the product. Electrical capacitance tomography (ECT) as a visualizing technique is one of the options to monitor the processes due to the advantages of fast imaging speed, non-intrusive and non-invasive, robust, withstanding high temperature and high pressure and low cost [1].

ECT has previously been used for fluidized-bed experiments for pharmaceutical processes [2]-[8]. Tanfara *et al.* evaluated the effect of particle size distribution on local voidage in a bench-scale conical fluidized bed dryer using a twin-plane ECT system [2]. Chaplin *et al.* implemented calibration of an ECT sensor for monitoring the fluidized bed drying of pharmaceutical granule [3]. Wiens *et al.* investigated the ECT for imaging a conical fluidized bed with dry pharmaceutical granule [4]. Wang *et al.* investigated the batch fluidized-bed drying with ECT, including the mathematical modeling, CFD simulation,

online measurement and control [5], [6] [7]. Rimpiläinen *et al.* estimated the moisture distribution and hydrodynamics of wet granules during fluidized bed drying and characterized with volumetric ECT [8].

All the researches mentioned above used ECT sensors with external electrodes (EE) only. As well known, because the sensitivity in the center of an EE sensor is weak, the images reconstructed by an EE sensor are usually blurred in the central area. To improve the image quality for a square-shape circulating fluidized bed (CFB), Liu *et al.* presented a square ECT sensor structure with internal-external electrodes (IEE) [9]. The IEE sensor can effectively increase the sensitivity in the central area. Rezvanpour *et al.* recently designed an ECT sensor with circular internal-external electrodes to investigate the droplet distribution in electrohydrodynamic atomization [10]. Apparently, they used the internal electrodes and external electrodes separately and hence the advantage of the IEE sensor was not fully utilized.

For some typical granulation, coating and drying processes, e.g. a Wurster tube coater, it is difficult to achieve a high contrast and spatial resolution to reveal the materials distribution in the concentric annulus, using a conventional EE sensor. To investigate the distribution of the fluid in an annulus area using ECT, a possibility is to use an IEE sensor. The effect of the number of electrodes and the measurement strategy in IEE senor evaluated by Ye and Yang [11] by numerical simulation.

In this paper, the IEE sensors with different configurations and with two measurement strategies are investigated by numerical simulation and experiment.

II. Numerical Simulation

A. Simulation arrangement

The IEE sensors with 12 external electrodes and 4 internal electrodes are utilized in both numerical simulation and experimental study. Fig. 1 shows three IEE sensors with different internal and external radius, where the ratio of radius of annular

area represented by R2:R3 is 0.3, 0.4 and 0.5, respectively. The covering ratio of electrodes is 90%.

To evaluate the influence of the internal shield, the IEE sensors with and without internal shield are used for comparison. The internal shield illustrated in Fig. 1 is placed on the internal wall of the internal tube. In that case, the internal wall is regarded as a shield layer.

Because the internal shield may affect the capacitance of the internal electrodes, two different measurement strategies, i.e. the external-internal (EI) strategy and the external-opposite-internal (EOI) strategy are considered. The total number of measurements with the EOI strategy is
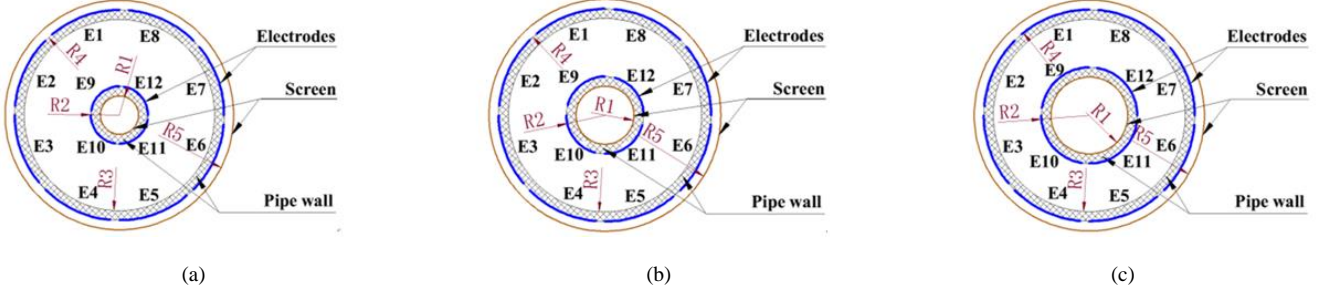

Fig. 1 ECT sensors for concentric annulus with dimensions. (a) R1:R2:R3:R4:R5 = 0.2:0.3:1.0:1.1:1.2. (b) R1:R2:R3:R4:R5 = 0.3:0.4:1.0:1.1:1.2. (c) R1:R2:R3:R4:R5 = 0.4: 0.5:1.0:1.1:1.2.

$$M = (N_E + N_I)(N_E + N_I - 1)/2 \quad (1)$$

where N_E is the number of external electrode and N_I is the number of internal electrode. The total number of measurements with the EO strategy is

$$M = N_E(N_E - 1)/2 + N_E \cdot N_I \quad (2)$$

In this study, $N_E = 12$ and $N_I = 4$. Using the EOI and EO strategies, the number of measurements is 120 and 114, respectively.

In some iterative algorithms and regularization algorithms, it is difficult to determine the number of iterations and the regularization parameter for different sensors and different permittivity distribution. Therefore, the linear back projection (LBP) algorithm is used throughout this work. The LBP algorithm [13] can be described as

$$\hat{\mathbf{g}} = G\left[\frac{\mathbf{S}^T \boldsymbol{\lambda}}{\mathbf{S}^T \mathbf{I}_\lambda}\right] \qquad \mathbf{I}_\lambda = [1,1,\cdots,1] \quad (3)$$

where $\hat{g}$ is the normalized permittivity vector, $\boldsymbol{\lambda}$ is the normalized change in the measured capacitance, $\mathbf{S}$ is the sensitivity matrix, $\mathbf{I}_\lambda$ is an identity vector. G is a projection operator given by

$$G[f(x)] = \begin{cases} 0 & f(x) < 0 \\ f(x) & 0 \le f(x) \le 1 \\ 1 & f(x) > 1 \end{cases} \quad (4)$$

The sensitivity map can be described as

$$S_{ij}(x,y) = -\iint_{p(x,y)} \frac{\nabla \phi_i(x,y)}{V_i} \cdot \frac{\nabla \phi_j(x,y)}{V_j} dxdy \quad (5)$$

where $S_{ij}(x,y)$ defines the sensitivity between the ith electrode and the jth electrode over the area $p(x,y)$, $\phi_i(x,y)$ is the potential distribution inside the sensing domain while the ith electrode is selected as an excitation electrode with a voltage V_i applied on it and the other electrodes are used as detection electrodes.

In simulation, ε_{low} and ε_{high} are 1.0 and 3.0 respectively. The permittivity of the pipe wall ε_{wall} is 2.6. The corresponding normalized permittivity distributions, including two annular distributions, two bar distributions and two stratified distributions, are illustrated in Fig. 2. The capacitance data can be obtained by numerical simulations. Both noise free data and noise-contaminated data with 50dB and 40dB noise are utilized. For each data vector of capacitance, the power of the noise free data is measured before adding the Gaussian noise. Modeling and imaging based on LBP are carried out using COMSOL Multiphysics™ and MatLab™.

The sensing domain is divided into fine meshes so that the voltage measurements are not changed if the number of elements is further increased. To assess the quality of image reconstruction in simulation, the relative image error and the correlation coefficient between the true permittivity distribution and the reconstructed images are used as criteria. The definition of the relative image error and the correlation coefficient can be seen in equations (6) and (7) [13], respectively.

The lower relative image error and the higher correlation coefficient mean good image reconstruction results.

$$\text{Image error} = \frac{\left\|\hat{\mathbf{g}} - \mathbf{g}\right\|}{\left\|\mathbf{g}\right\|} \times 100\% \tag{6}$$

$$\text{Correlation coefficient} = \frac{\sum\limits_{i=1}^{N_p}\left(\hat{g}_i - \bar{\hat{\mathbf{g}}}\right)\left(g_i - \bar{\mathbf{g}}\right)}{\sqrt{\sum\limits_{i=1}^{N_p}\left(\hat{g}_i - \bar{\hat{\mathbf{g}}}\right)^2 \sum\limits_{i=1}^{N_p}\left(g_i - \bar{\mathbf{g}}\right)^2}} \tag{7}$$

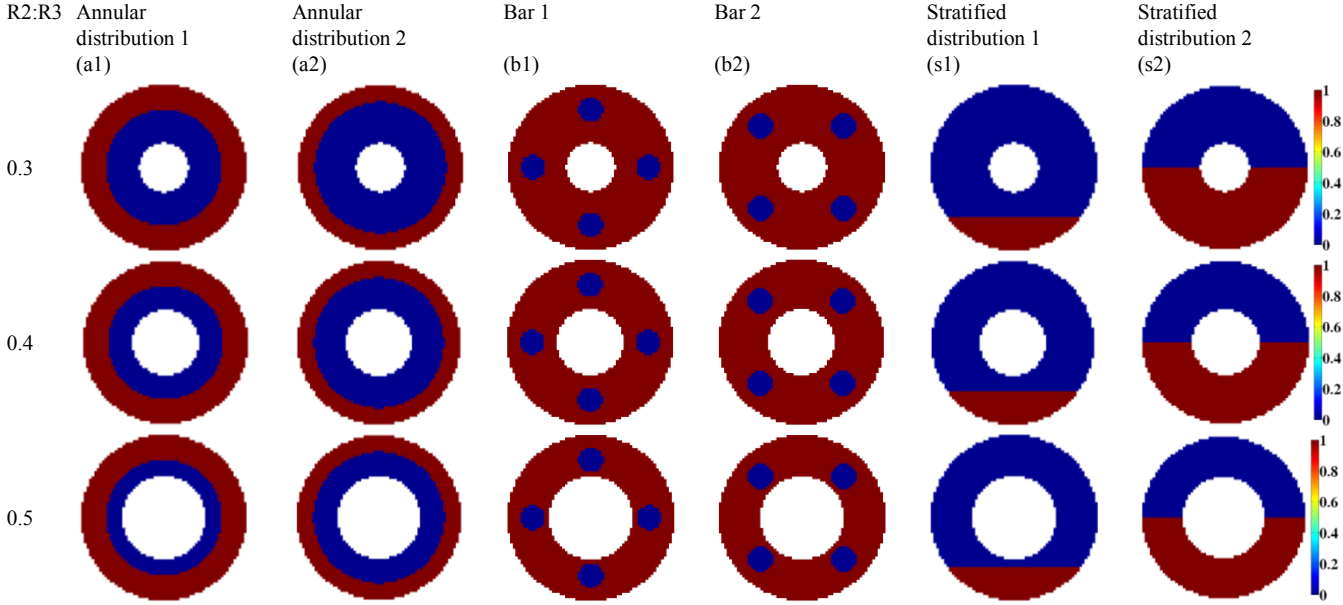where N_p is the number of the pixels in the sensing domain.

Fig. 2 Permittivity distributions for simulation.

B. Results and Discussion

1) With Noise free data

Fig. 3 shows the images reconstructed from the noise free capacitance data. Fig. 4 illustrates the quantitative results, including the image error and the correlation coefficient.
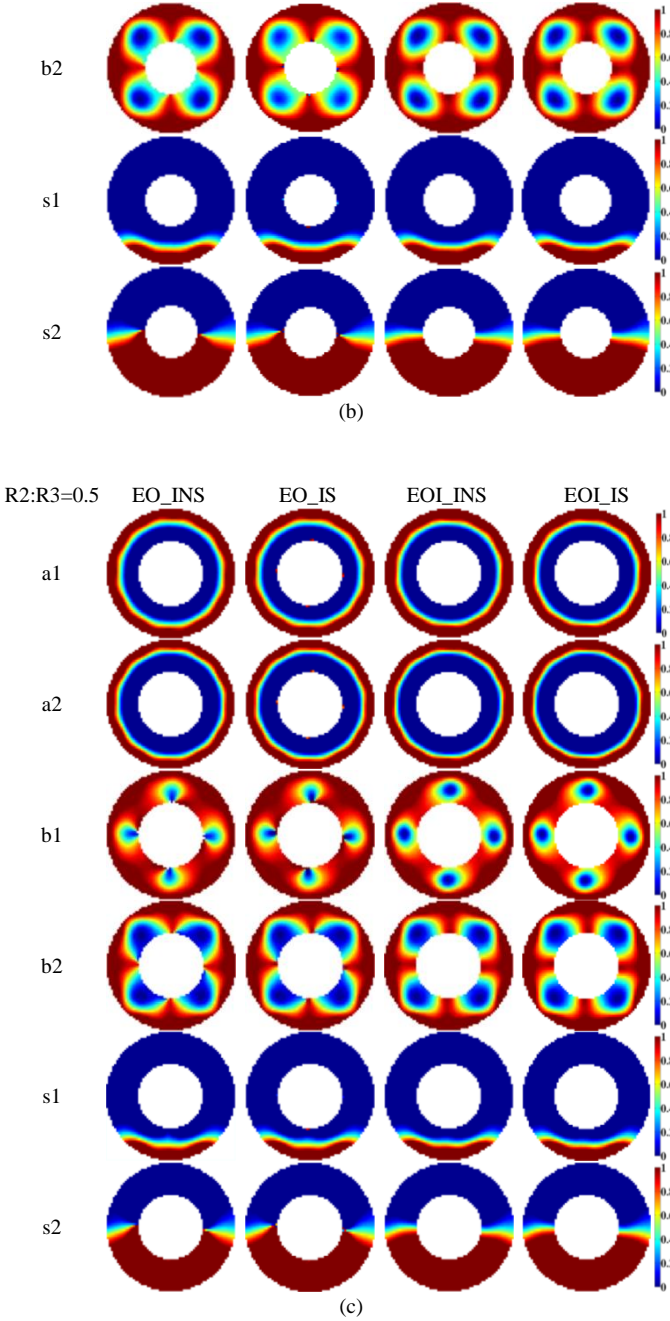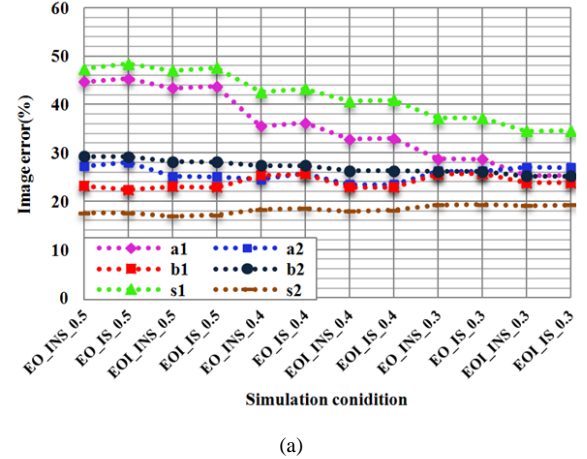
(b)

R2:R3=0.5   EO_INS   EO_IS   EOI_INS   EOI_IS

(c)
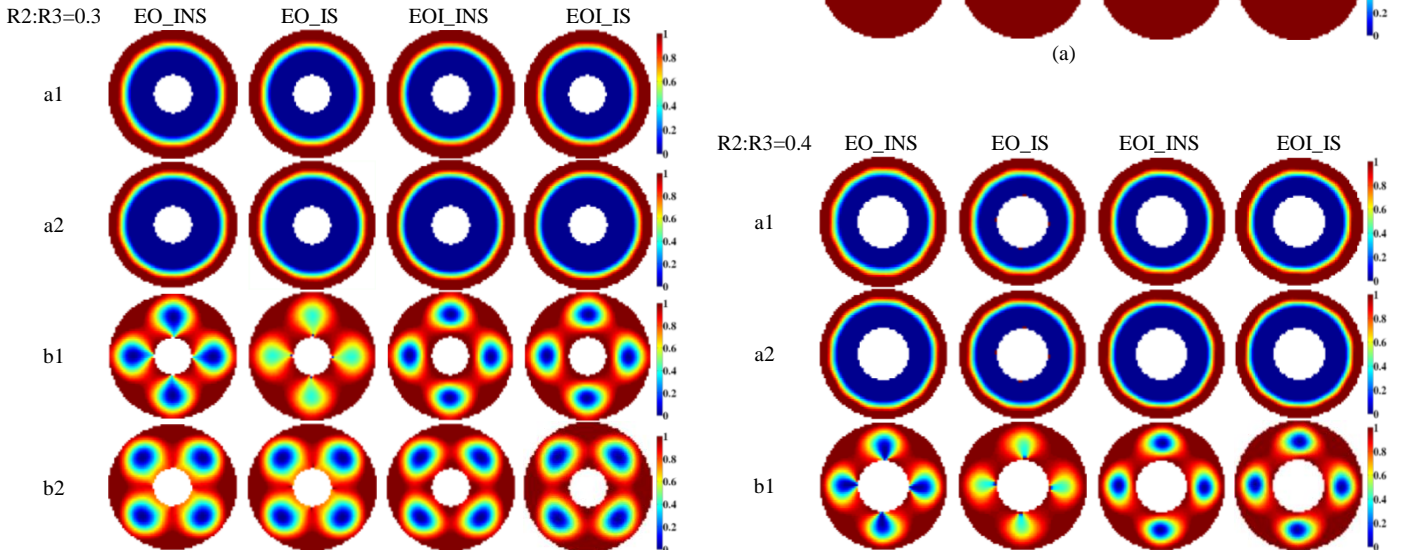
Fig. 3 Images reconstructed using noise free data from the sensors with different configurations. (a) R2:R3 = 0.3. (b) R2:R3 = 0.4. (c) R2:R3 = 0.5.

From the reconstructed images shown in Fig. 3, it can be seen that the images reconstructed for bar distributions with the EOI strategy have higher image contrast and spatial resolution than that with the EO strategy. For the annular and stratified distributions, the image contrast and spatial resolution have no significant difference. Using the noise free data, the internal shield has almost no influence on the imaging property of the IEE sensors.

Fig. 4 (a) shows that the image errors for the bar distributions, annular distribution 2 and stratified distribution 1 have a little variation with the change in the measurement strategy and the ratio of radius of concentric annulus. For bar distribution 1 and

stratified distribution 2, the image errors are decreased significantly with the decrease in the ratio of radius of concentric annulus. To be more specific, the image errors with the EOI measurement strategy are less than that with the EO measurement strategy, for almost the all cases. The correlation coefficients illustrated in Fig. 4 (b) show that the variation tendency of correlation coefficient is exactly the same with the image error for both the annular distributions and stratified distributions. For annular distribution 2 and stratified distribution 2, the correlation coefficients are stable with different measurement strategies and the ratio of radius of concentric annulus. In contrast, the correlation coefficients for the annular distribution 1 and stratified distribution 1 are increased with the decrease in the ratio of radius of concentric annulus. For bar distribution 2, the correlation coefficients with the same measurement strategy are increased with the decrease in the ratio of concentric annulus. However, the correlation coefficients for the bar distribution 1 are decreased with the decrease in the ratio of radius of concentric annulus. The possible reason is the asymmetric configuration of the IEE sensor. The quantitative analysis also indicates that the correlation coefficients with the EOI measurement strategy are greater than that with the EO measurement strategy.

(a)
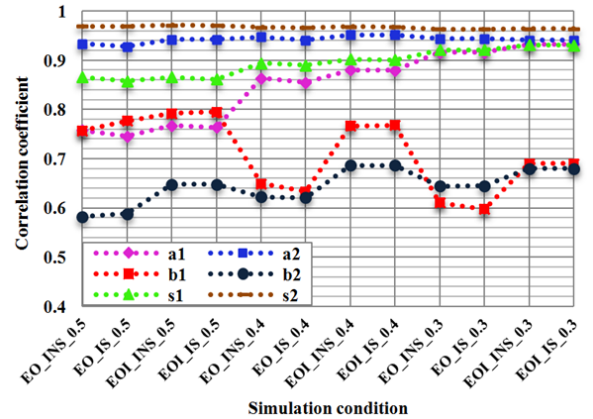
(b)

Fig. 4 Quantitative results obtained from noise free data. (a) Image error. (b) Correlation coefficient.

2) With 50 dB noise data

To compare the performance of the IEE sensors designed in this work, and the influence of the measurement strategies and the internal shield, the capacitance data with 50 dB Gaussian noise are generated for image reconstruction. Fig. 5 shows the images reconstructed from the 50dB noise data. Fig. 6 illustrates the quantitative results including the image error and correlation coefficient.
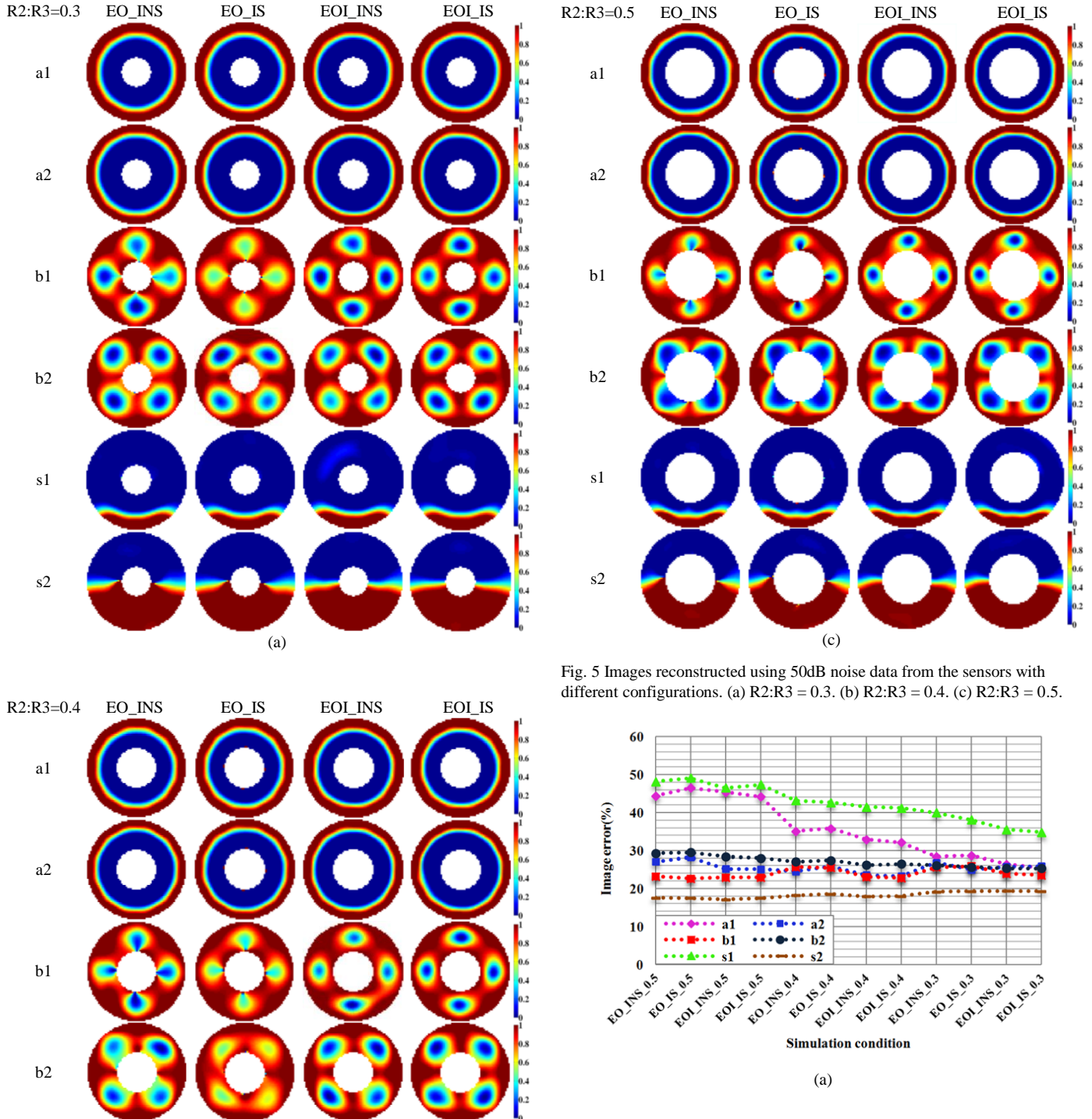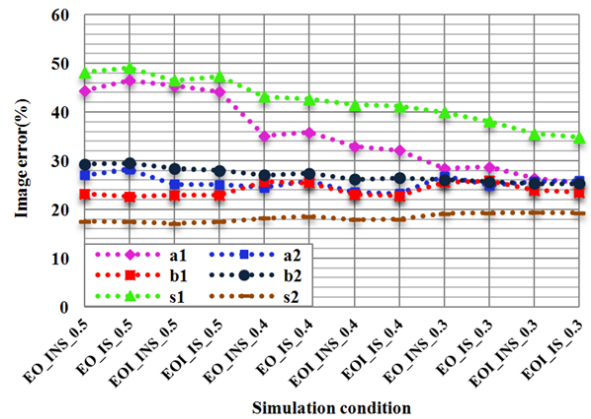

(a)

(b)

(c)

Fig. 5 Images reconstructed using 50dB noise data from the sensors with different configurations. (a) R2:R3 = 0.3. (b) R2:R3 = 0.4. (c) R2:R3 = 0.5.
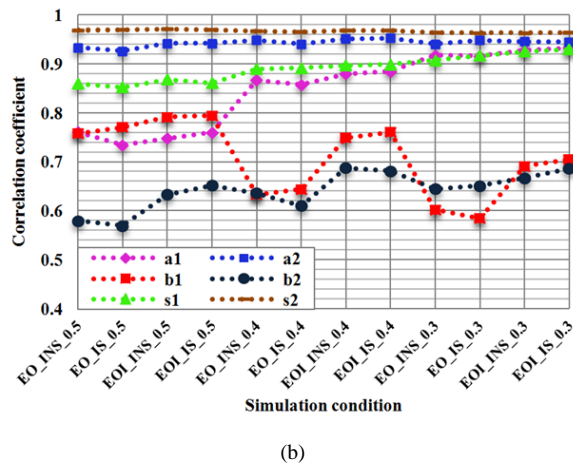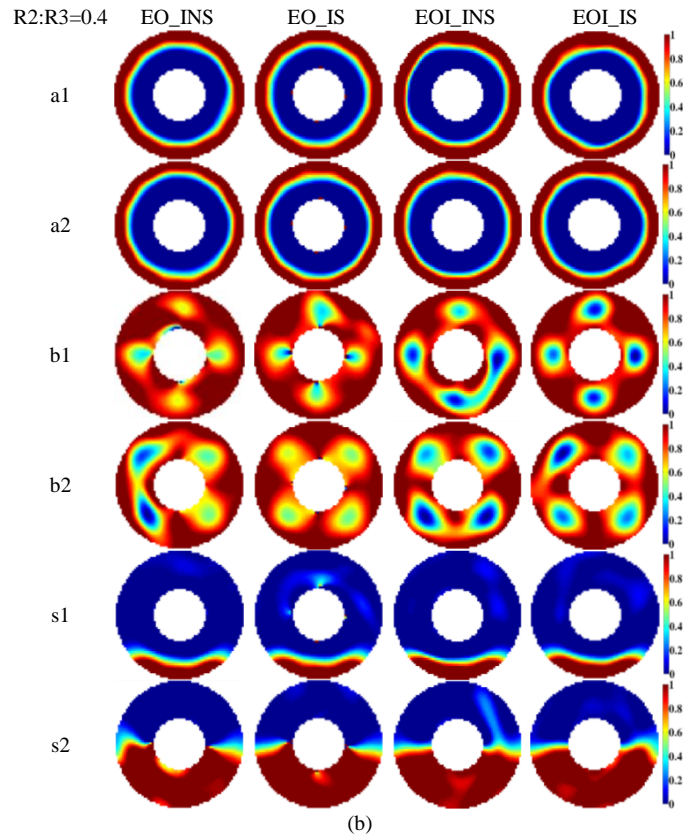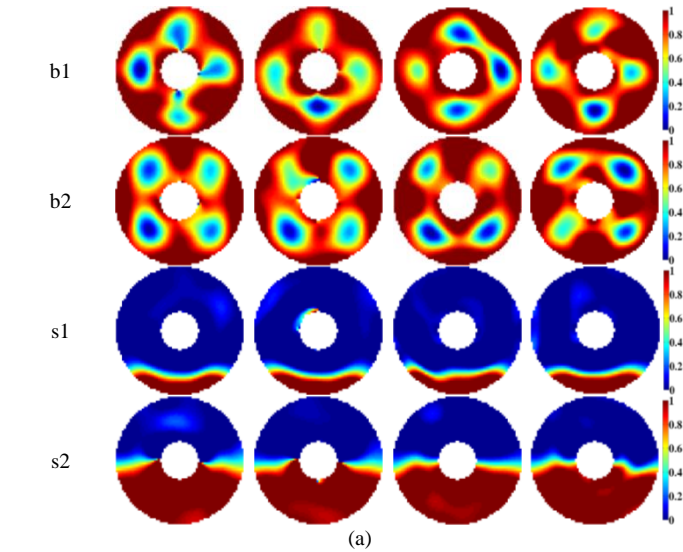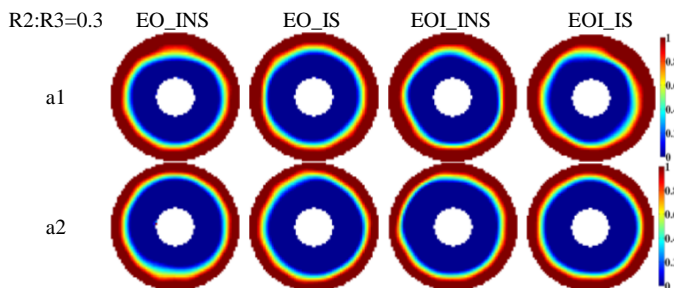

(a)

(b)

Fig. 6 Quantitative results obtained from 50dB noise data. (a) Image error. (b) Correlation coefficient.

In comparison to the images reconstructed from the noise free data, the image contrast and spatial resolution of the images shown in Fig. 5 is decreased significantly, especially for the bar distributions. However, the images reconstructed for the bar distributions with the EOI strategy also have higher image contrast and spatial resolution than that with the EO strategy. For the annular and stratified distributions, the image contrast and spatial resolution have not obvious fluctuation with the change in the measurement strategy and the internal shield.

The variation tendency of the image errors and the correlation coefficients from the 50 dB noise data are similar to that from the noise free data. For stratified distribution 1 and annular distribution 1, the image quality is increased with the decrease in the ratio of radius of concentric annulus. For bar distribution 2, the quality of the images with the same measurement strategy is increased with the decrease in the ratio of radius of concentric annulus. In comparison to bar distribution 2, the image quality for bar distribution 1 is decreased with the decrease in the ratio of radius of concentric annulus while using the same measurement strategy. Specifically, the image quality with the EOI measurement strategy is better than that with the EO measurement strategy.

3) With 40 dB noise data

In this comparative study, the signal-to-noise ratio is reduced to 40 dB. Fig. 7 shows the images reconstructed from the 40dB noise data. Fig. 8 plots the image errors and correlation coefficients.
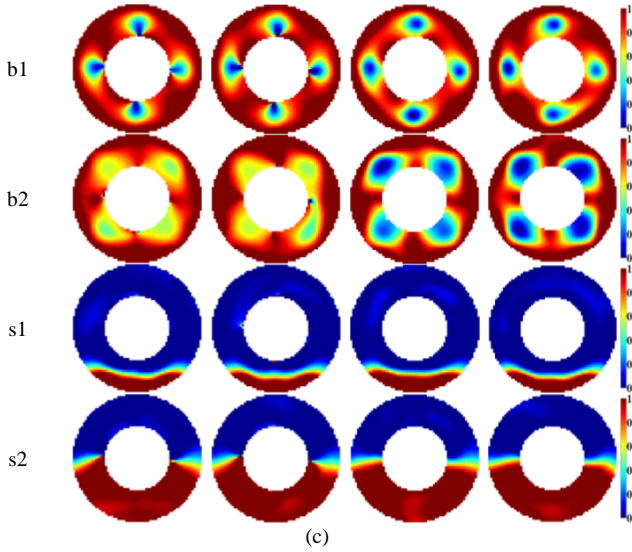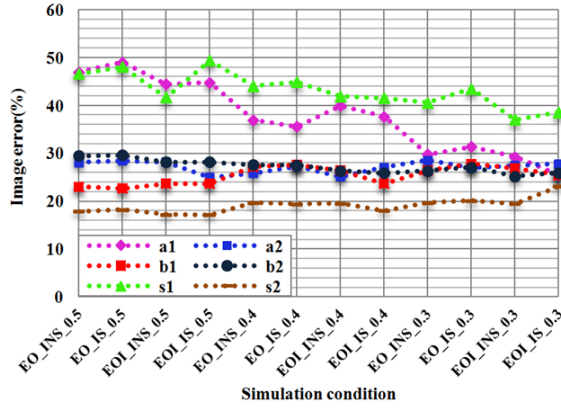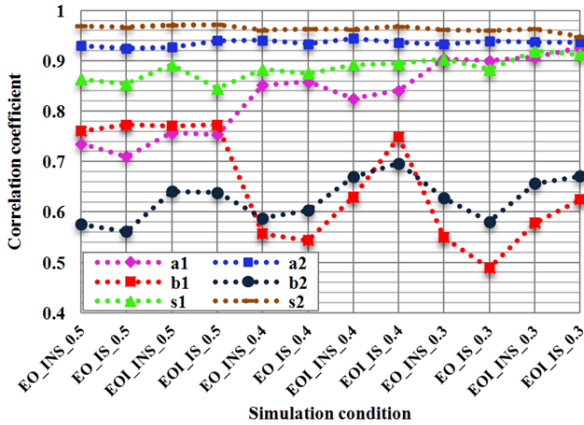
Fig. 7 Images reconstructed using 40dB noise data from the sensors with different configurations. (a) R2:R3 = 0.3. (b) R2:R3 = 0.4. (c) R2:R3 = 0.5.

(a)

(b)

Fig. 8 Quantitative results obtained from 40dB noise data. (a) Image error. (b) Correlation coefficient.

From Fig. 7, it can be clearly seen that the images reconstructed from the 40 dB noise data have serious distortions, especially for the bar distributions. The image contrast and spatial resolution of the images reconstructed for the annular distributions and stratified distributions are also significantly lower than that

from the noise free and 50 dB noise data. One example of the influence of noise level is shown in Fig. 9. The image errors are calculated for three permittivity distributions, including annular distribution 1, bar distribution 1 and stratified distribution 1, with the EOI measurement strategy and a ratio of radius of concentric annulus of 0.3. From Fig. 9, it can be seen that the image errors from the 40 dB noise data are significantly higher than that from the 50 dB noise data and noise free data.

The influence of the internal shield on the images of the IEE sensor is not obvious either. For bar distributions, the image contrast and spatial resolution with the EOI strategy is better than that with the EO strategy. For other distributions, the effect of the measurement strategies is not obvious.

As shown in Fig. 8, although the fluctuation of the quantitative results is more frequent than that with the noise free and 50 dB noise data, the overall tendency of the distribution of the data points is similar. With the LBP algorithm, the EOI measurement strategy also has a higher imaging quality than the EO strategy.
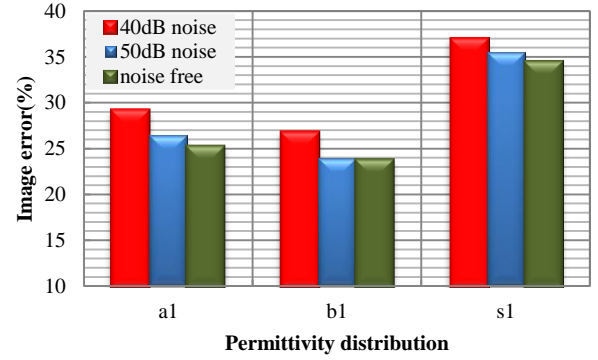

Fig. 9 Image errors for three permittivity distributions with EOI measurement strategy while R2:R3 = 0.3.

III. EXPERIMENTAL EVALUATION

A. Experimental Setup

An ACECT system with 16 channels from ECT Instruments Ltd, Manchester, UK, is used in the experiment. The ECT measurement system can be seen in Fig. 10 including an IEE sensor (Sensor1) designed in this work. Three ECT sensors with the same covering ratio of 90% are designed and utilized for comparison. The models of three ECT sensors are illustrated in Fig. 11. The first two ECT sensors in Fig. 11 have 12 external electrodes and 4 internal electrodes, where the ratio of radius of annulus area is 0.36 (Sensor1) and 0.5 (Sensor2), respectively. The third ECT sensor (Sensor3) has only 12 external electrodes. The IEE sensors are designed with and without internal shield respectively.

1.ECTmeasurement system; 2.Data acquisition and image reconstruction software; 3.ECT sensor.
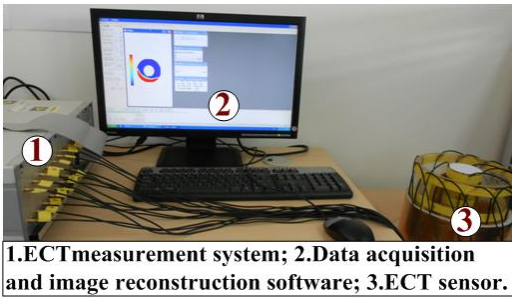
(a)
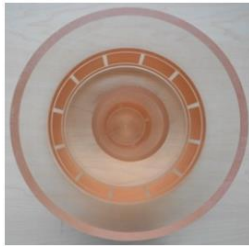
(b)

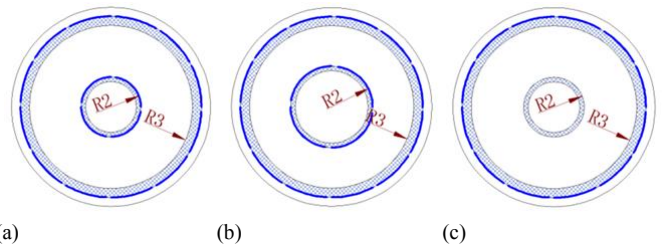Fig. 10 ECT measurement system and sensor. (a) ECT measurement system. (b) Sensor 1.

(a)   (b)   (c)

Fig. 11 Models of ECT sensors used in experimental studies. (a) Sensor1, IEE, R2:R3 = 0.36. (b) Sensor2, IEE, R2:R3 = 0.5. (c) Sensor3, EE, R2:R3 = 0.36.

The real permittivity distribution can be seen in Fig. 12. To display the permittivity distributions more clearly, the corresponding models of the real permittivity distributions are also given in Fig. 12. The LBP algorithm is utilized for the image reconstruction. The EO and EOI measurement strategies are considered for comparison.

B. Experimental Results

Nine groups of experimental results from the ECT sensors with different configuration and different measurement strategies are shown in Fig. 12. Considering the permittivity distributions are not exactly the same for one distribution in every test, the quantitative comparison is not evaluated.
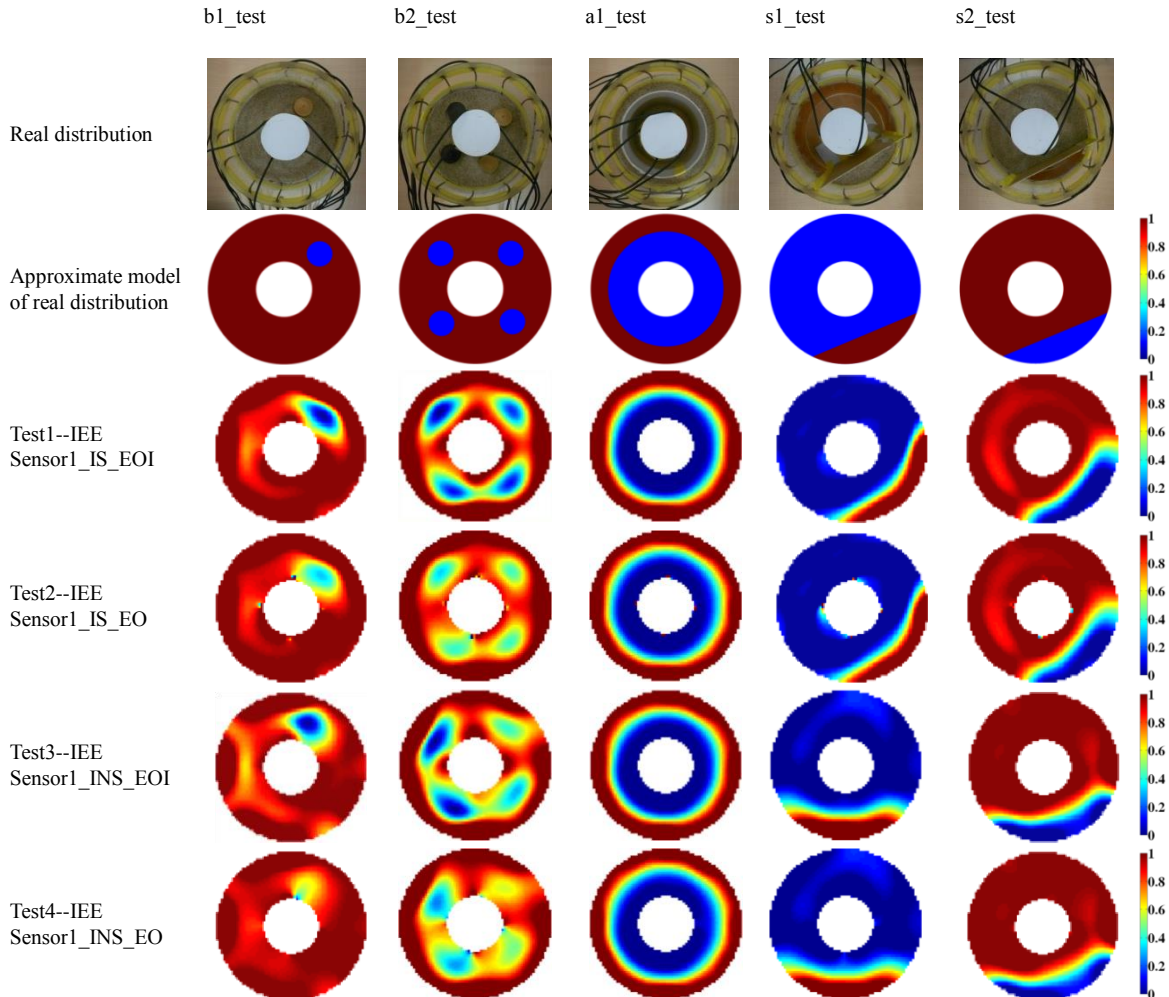
Fig. 12 Experimental results.

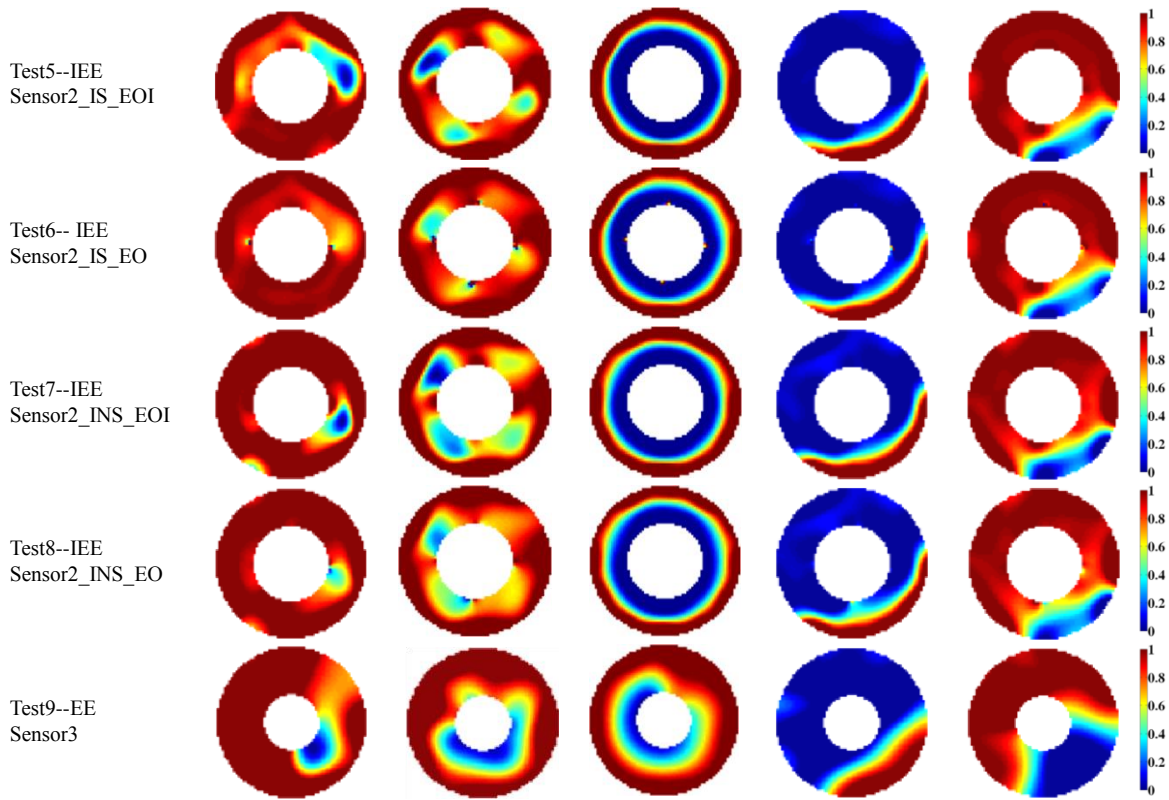From the experimental results in Test1, it can be seen that the images reconstructed from sensor1 with internal shield and the EOI measurement strategy have higher contrast and spatial resolution comparing with the images in Test2. Instead of the EOI strategy, the EO strategy is utilized in Test2. The experimental results in Test1 and Test2 indicate that the images reconstructed from sensor1 with internal shield and the EO measurement strategy present obvious artifacts near the internal wall. In the meanwhile, the image contrast and spatial resolution of the reconstructed images is increased significantly, especially for the permittivity distribution of b1_test and b2_test. For permittivity distribution of a1_test, s1_test and s2_test, the quality of the images has been less affected by the using of the EO strategy.

The experimental setup in Test3 and Test1 is basically the same except for the internal shield. In Test3, the IEE sensor1 has no the internal shield. Comparing with the experimental results in Test1, the quality of the images reconstructed from sensor1 without internal shield is not decreased or increased significantly. The images reconstructed in Test3 with the EOI measurement strategy also have higher contrast and spatial resolution than the images reconstructed in Test4 with the EO measurement strategy. Without internal shield, the images reconstructed from sensor1 with the EO measurement strategy have no artifacts near the internal wall.

In test5, the sensor2 is utilized in the experimental studies. For the sensor2, the ratio of radius of annulus area is designed as 0.5. The images reconstructed from the sensor2 with internal shield and EOI measurement strategy also have a high contrast

and spatial resolution for most permittivity distributions. However, for the permittivity distribution of b2_test and s2_test, the image quality is reduced significantly comparing with the images reconstructed in Test1 and Test3. With the EO measurement strategy in Test6, the image contrast and the spatial resolution are decreased significantly for almost all of the permittivity distributions except a1_test. In the meanwhile, the artifacts can be found near the internal wall.

In Test7 and Test8, the sensor used in the experimental studies is the senor2 is without internal shield. The images reconstructed in Test7 and Test8 present similar quality to the images reconstructed in Test5 and Test6. The quality of the images with the EOI strategy is also higher than that with the EO strategy. As there is no internal shield in Test8, the reconstructed images near the internal wall have no artifacts either.

To demonstrate the advantage of the IEE sensor, an EE sensor with 12 external electrodes is designed for Test9. From the experimental results of Test9, it can be seen that only the image reconstructed for the permittivity distribution s1_test has a high image contrast and spatial resolution but it is still not better than that in Test1 and Test3. For other permittivity distributions, the reconstructed images have serious distortions and lower image contrast and spatial resolution. It is difficult to reconstruct the permittivity distributions far away from the external wall using the EE sensor.

C. *Signal-to-noise ratio (SNR) analysis*

SNR is introduced to evaluate the quality of the capacitance data. Hu and Yang [12] defined the SNR in ECT system for the measured capacitance as

$$\text{SNR} = 20\log10\left(\frac{\text{Signal}}{\text{Noise}}\right) = 20\log10\sqrt{\frac{\sum_{i=1}^{N_F}C_i^2}{\sum_{i=1}^{N_F}\left(C_i - \overline{C}\right)^2}} \qquad (8)$$

where, N_F is the number of measurement frames, C is the measured capacitance from an electrode pair and $\overline{C}$ is the average of measured capacitance.

Fig. 13 shows the SNR distribution of the measured capacitance from different electrode pairs for two permittivity distributions, including a bar distribution and a stratified distribution utilized in the test. The x-coordinate axis consists of the number of excitation electrode and detection electrode. For example, 13-14 means that E13 and E14 are selected as the excitation and detection electrode, respectively. The SNR distribution for two permittivity distributions shows the same trend. If an external electrode is selected for excitation, the SNR of the measured capacitance from the sensor with the internal shield is higher than or equal to that without the internal shield. On the contrary, if an internal electrode is utilized for excitation, the SNR from the internal electrode pairs of the sensor without the internal grounded is higher than that with the internal shield. In comparison, the SNR of the EE senor is significantly lower than that of the IEE sensors, including sensor1 and sensor2.
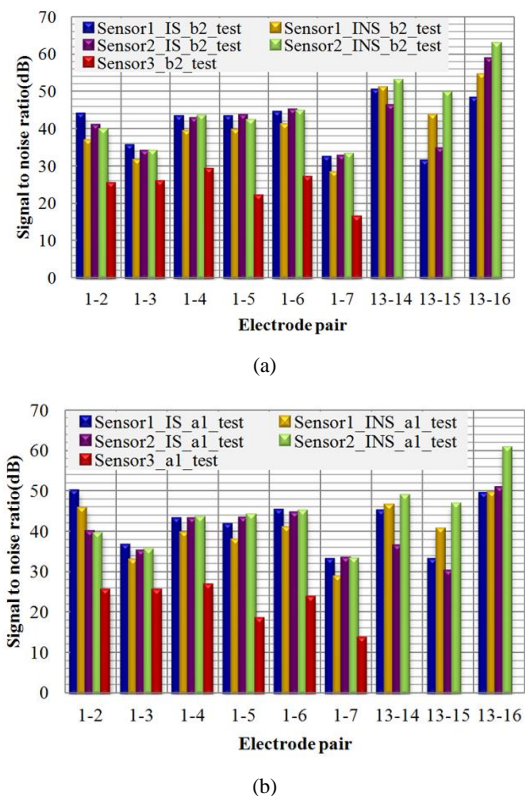

(a)

(b)

Fig. 13 SNR of the measured capacitances from different electrode pairs for two permittivity distributions. (a) Bar distribution 2 used in test. (b) Annular distribution 1 used in test.

IV. Conclusions

By considering the influence of the ratio of radius of concentric annulus, the measurement strategy and the internal shield, the performance of IEE sensors is discussed based on the LBP algorithm by numerical simulation and experiment.

For numerical simulation, the noise free, 50 dB noise and 40 dB noise data are used for comparison. The simulation results with 6 IEE sensors with different internal and external radius show that the image quality is increased with the decrease in the ratio of radius of concentric annulus. The internal shield has almost no effect on the image reconstruction. With the LBP algorithm, the EOI measurement strategy can reconstruct the image with higher quality than the EO measurement strategy.

In experimental studies, 2 IEE sensors with different ratio of radius of concentric annulus and 1 EE senor are used. The experimental results are in agreement with the simulation. The IEE sensors with a small ratio of radius of concentric annulus have a good imaging property and the EOI measurement strategy outperforms the EO strategy. The images reconstructed from the IEE sensors have higher image contrast and spatial resolution than the EE sensor. The experimental results indicate that the capacitance measured from the internal electrodes of the IEE sensors without internal shield have higher SNR than that with internal shield.

In summary, both the simulation and experimental results show that the IEE sensor with a smaller ratio of radius of concentric annulus and the EOI measurement strategy has obvious advantage over other ECT sensors and measurement strategies studied in this work. The internal shield has a negative effect on the quality of measurements when an external electrode or internal electrode is selected for excitation.

References

[1] W. Q. Yang, Design of electrical capacitance tomography sensors, *Meas. Sci. and Technol.*, vol.21, no.4, pp 1-13, 2010.

[2] H. Tanfara, T. Pugsley and C.Winters, Effect of particle size distribution on local voidage in a bench-scale conical fluidized bed dryer, *Drying Technol.* vol.20, no.6, pp.1273-1289, 2002.

[3] G. Chaplin, T. Pugsley, L. van der Lee, A. Kantzas and C. Winters, The dynamic calibration of an electrical capacitance tomography sensor applied to the fluidized bed drying of pharmaceutical granule. *Meas. Sci. Technol.* vol.16, no.6, pp.1281-1290, 2005.

[4] J. Wiens and T. Pugsley, Tomographic imaging of conical fluidized bed of dry pharmaceutical granule, *Powder Technol.* vol.169, no.1, pp.49-59, 2006.

[5] H.G. Wang, W.Q. Yang, P.R. Senior, R.S. Raghavan and S.R. Duncan, Investigation of batch fluidized-bed drying by mathematical modeling, *CFD simulation and ECT measurement. AIChE J.*, vol.54, no.2, pp.427-444, 2008.

[6] H.G. Wang, P.R. Senior, R. Mann and W.Q. Yang, Online measurement and control of solids moisture in fluidized bed dryers, *Chem. Eng. Sci.*, vol.64, no.12, pp.2893-2902, 2009.

[7] H.G. Wang and W.Q. Yang, Measurement of fluidised bed dryer by different frequency and different normalisation methods with electrical capacitance tomography, *Powder Technol.* vol.199, no.1, pp.60–69, 2010.

[8] V. Rimpiläinen, L. M.Heikkinen and M. Vauhkonen, Moisture distribution and hydrodynamics of wet granules during fluidized-bed drying characterized with volumetric electrical capacitance tomography, *Chemical Engineering Science*, vol.75, pp.20-234, 2012.

[9] S. Liu, W. Q. Yang and H. Wang, An electrical capacitance tomography sensor with internal-external electrodes, *Proc. SPIE*, vol. 4188, pp.300-307, 2001.

[10] A. Rezvanpour, C. Wang, Y. Liang and W. Q. Yang, Investigation of droplet distribution in electrohydrodynamic atomization (EHDA) using an ac-based electrical capacitance tomography (ECT) system with an internal-external electrode sensor, *Meas. Sci. Technol.*, vol.23, no.1, pp.1-10, 2012.

[11] J. M. Ye and W. Q. Yang, Evaluation of electrical capacitance tomography sensors for concentric annulus, *IEEE Sensors Journal*, vol.13, no.2, pp.446-456, 2013.

[12] X.H. Hu and W.Q. Yang, Design of a data acquisition and function generation unit with USB, *Meas. Sci. Technol*. vol.17, no.4, N17–23, 2006.

[13] W.Q. Yang and L.H. Peng, Image reconstruction algorithms for electrical capacitance tomography, *Meas. Sci. Technol.*, vol.14, no.1, pp. R1-R13, 2003.